Bent Domain Structure of Recombinant Human IgE-Fc in Solution by X-ray and Neutron Scattering in Conjunction with an Automated Curve Fitting Procedure†

Andrew J. Beavil,‡,§ Robert J. Young,‡ Brian J. Sutton,‡ and Stephen J. Perkins*,§

Randall Institute, King's College London, 26-29 Drury Lane, London WC2B 5RL, U.K., and Department of Biochemistry and Molecular Biology, Royal Free Hospital School of Medicine, Rowland Hill Street, London NW3 2PF, U.K.

Received June 22, 1995; Revised Manuscript Received August 30, 1995⊗

ABSTRACT: Human immunoglobulin E (IgE) consists of 14 domains, each with the characteristic immunoglobulin fold structure. Compared with the 12-domain structure of immunoglobulin G (IgG), IgE has an additional pair of domains (Cε2) in the Fc region in place of the hinge of IgG. The crystal structure of the 4-domain Fc fragment of IgG is known, but not that of the 6-domain Fc fragment of IgE (IgE-Fc). In order to elucidate the position of the Cε2 domains in the domain structure of IgE-Fc, IgE-Fc was studied by synchrotron X-ray and pulsed neutron scattering. The upper limit on the X-ray radius of gyration R_G which determines macromolecular elongation was determined to be 3.52 ± 0.14 nm. That for the neutron R_G (measured in 100% ^2H_2O buffers) was 3.53 ± 0.05 nm. The X-ray and neutron cross-sectional radii of gyration were 1.89 ± 0.05 and 1.56 ± 0.09 nm, respectively. The scattering curves were modeled on the basis of a previously-predicted model for IgE-Fc (Helm, B. A., Ling, Y., Teale, C., Padlan, E. A., & Brüggemann, M. (1991) *Eur. J. Immunol. 21,* 1543−1548). The extended arrangement of domains in that model resulted in poor agreement with experimental data. Interactive and automated procedures for the fitting of crystallographically-derived domain models to scattering data were developed. Each pair of Cε2, Cε3, and Cε4 domains was translated and rotated relative to the remaining structure in a comprehensive five-parameter search of more than 37 000 models. Substantially improved agreement between the experimental and calculated scattering curves was obtained. Bent models for IgE-Fc in which the Cε2 domain pair is rotated by at least 40−50° from its position in the previously predicted linear IgE model consistently gave the best agreement with the X-ray and neutron scattering curves. Such a structure for the Fc fragment accounts in part for the bent structure previously proposed for intact human IgE, which is important for understanding the interaction between IgE and its receptors.

The plasma protein immunoglobulin E (IgE)[1] plays a key recognition role in the immune response to foreign antigenic material and the development of an allergic, inflammatory response (Sutton & Gould, 1993). It is monomeric and contains 14 immunoglobulin (Ig) fold domains in 4 polypeptide chains (Figure 1), in contrast to the principal antibody class immunoglobulin G (IgG), which contains 12 domains. The "extra" pair of domains $(C\epsilon2)_2$ in IgE replaces the hinge region of IgG and in this respect is similar to the structure of the subunit of immunoglobulin M. The interaction between IgE and its high affinity receptor FcεRI on mast cells and basophils is central to allergic disease (Sutton & Gould, 1993) and is notable for its high affinity. The association constant $K_a \approx 10^{10}$ M^{-1} is over an order of magnitude greater than that for antibodies of any other class with any known Fc receptor (Ravetch & Kinet, 1991). IgE interacts with FcεRI through its Fc region at the Cε3 domain,

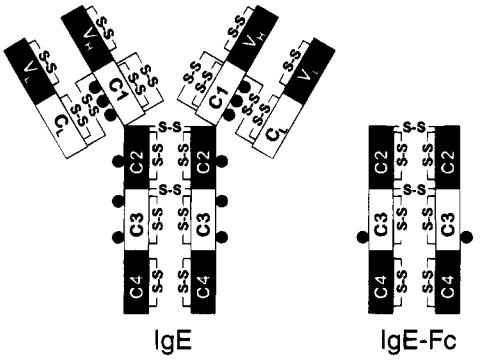

FIGURE 1: Schematic diagram of the immunoglobulin fold domains in the structure of IgE. Each heavy chain in IgE contains the V_H, Cε1, Cε2, Cε3, and Cε4 domains, each of which is represented by a rectangle and S−S to designate the internal disulfide bridge. Each light chain contains the V_L and C_L domain. Pairs of heavy chains are disulfide-linked twice between the Cε2 domains at Cys241−Cys241 and Cys328−Cys328. The six putative oligosaccharide sites per heavy chain are marked by filled circles. Recombinant IgE-Fc contains the Cε2, Cε3, and Cε4 domains in which the oligosaccharide sites at Asn265 in Cε2 and Asn371 in Cε3 have been removed, but leaving intact that at Asn394 in Cε3.

including the region adjacent to the Cε2 domain (Helm et al., 1988; Weetall et al., 1990; Nissim et al., 1991, 1993; Beavil et al., 1993; Presta et al., 1994). Thus for IgE and its Fc fragment IgE-Fc, the solution structure of the $(C\epsilon2)_2$ domains relative to those of the $(C\epsilon3)_2$ domains is of great

† S.J.P. acknowledges support from the Wellcome Trust, the Biotechnology and Biological Sciences Research Council, and the Royal Society. A.J.B. and B.J.S. thank the Science and Engineering Research Council for a studentship, and the National Asthma Campaign (U.K.), the Medical Research Council, and Apollon Inc. for further support.

* To whom correspondence and requests for reprints should be addressed.

‡ Randall Institute.

§ Royal Free Hospital School of Medicine.

⊗ Abstract published in *Advance ACS Abstracts,* October 15, 1995.

[1] Abbreviations: immunoglobulin E, IgE; recombinant Fc fragment of IgE, IgE-Fc; high affinity receptor of IgE, FcεRI.

0006-2960/95/0434-14449$09.00/0

interest for understanding IgE−receptor interactions.

By analogy with electron microscopy and X-ray studies of IgG and other immunoglobulin classes, IgE is expected to have an extended Y-shaped structure of two Fab regions, each consisting of V_L, V_H, C_L, and Cϵ1 domains, and one Fc region consisting of pairs of Cϵ2, Cϵ3, and Cϵ4 domains (Figure 1). In solution, fluorescent labeling shows that the distance between the V and Cϵ4 domains in IgE is 6.9 nm. This is considerably less than the distance of 17.5 nm expected for an extended planar molecule and suggests that these domains approach each other in a bent structure (Holowka et al., 1990; Zheng et al., 1991, 1992). No explanation for the existence of such a bent structure is available at present.

Solution scattering provides a multiparameter structural characterization of the domains in multidomain proteins under near-physiological conditions (Glatter & Kratky, 1982; Perkins, 1994). Interpretation is much improved if scattering curves are modeled using constraints based on the assembly of homologous crystal structures using molecular graphics and an algorithm that has been tested with known crystal structures (Smith et al., 1990; Perkins et al., 1993). Such a procedure can be automated (Mayans et al., 1995). All the domains in IgE display the immunoglobulin fold of known atomic structure (Williams & Barclay, 1988), and models for the structure of IgE-Fc have been predicted (Padlan & Davies, 1986; Helm et al., 1991). We report X-ray and neutron scattering data for recombinant IgE-Fc (Figure 1). An automated procedure was developed for comparison of the experimental scattering curves with those calculated from all possible relative domain structures for IgE-Fc, starting from the coordinates available from one of the existing two models for IgE-Fc (Helm et al., 1991). In contrast to the extended structure of Helm et al. (1991), we show that only a more compact or bent structure for IgE-Fc is consistent with the experimental data. Reasons for the existence of such a structure are considered, and the functional implications for IgE−receptor interactions are discussed.

MATERIALS AND METHODS

(a) Preparation of Human Recombinant Fc Fragment. IgE-Fc was expressed using a Chinese hamster ovary cell line (Young et al., 1995). It differs from the native sequence in having the N-terminal Cys225 replaced by Ala and the two surface-exposed ϵ-specific N-glycosylation sites on the Cϵ2 and Cϵ3 domains, Asn265 and Asn371, replaced by Gln (Figure 1). The conserved N-glycosylation site at Asn394 is retained (Figure 1). In addition, there is an N-terminal extension of two amino acids (Asp and Ile), resulting from cleavage of the genetically engineered leader sequence. The recombinant protein was isolated by affinity chromatography. The IgE-Fc culture supernatant was passed over an anti-IgE-Fc mAb 7.12−Sepharose 4B affinity column (Sherr et al., 1989), and the protein was eluted with 0.1 M glycine at pH 2.5, which was immediately neutralized with 1 M Tris.

(b) Sample Preparation for Solution Scattering. The samples were freed from nonspecific aggregates shortly before data collection by high performance liquid chromatography using a Pharmacia TSK G3000SW column in a mobile phase consisting of 200 mM Tris, pH 8.4, with 130 mM NaCl and 0.01% NaN_3. Samples were stored at 4−6 °C until required. Scattering experiments on IgE-Fc were performed using Dulbecco's phosphate buffer A (12.5 mM sodium phosphate, 140 mM NaCl at pH 7). X-ray work utilized H_2O buffers while the neutron work involved dialysis at 6 °C into the corresponding buffer in ^2H_2O for at least 36 h with four buffer changes. Sodium dodecyl sulfate−polyacrylamide gel electrophoresis under nonreducing conditions was used to verify the integrity of the samples. X-ray and neutron data collection was performed at 15 °C using a thermostated sample holder or rack.

(c) Composition of IgE-Fc. The amino acid composition of IgE-Fc was derived from the three C-terminal domains in the heavy chain sequence from the IgE myeloma protein ND (SwissProt Entry EPC$HUMAN). The sequence was initiated at DIVASRDFTPP... and ended at the C-terminus ...PGK. Asn265 and Asn371 were changed to Gln. The Fc fragment of native IgE has carbohydrate sites at Asn265 (Cϵ2 domain), and at Asn371 and Asn394 (Cϵ3 domain). Only that at Asn394 is occupied in recombinant IgE-Fc and is fully glycosylated (Young et al., 1995). Its composition was taken to be complex-type and similar to that determined by Rademacher et al. (1983) for IgG. This resulted in 650 amino acid and 18 carbohydrate residues, of dry volumes 92.0 and 3.5 nm^3, respectively, with a total molecular weight of 75 300 and partial specific volume of 0.728 mL/g (Perkins, 1986). Concentrations for molecular weight calculations were calculated from optical density measurements at 280 nm using an absorption coefficient of 13.2 (280 nm, 1%, 1 cm) calculated from the protein and carbohydrate composition by the corrected Wetlaufer procedure (Perkins, 1986).

(d) X-ray Data Collection at the Synchrotron Radiation Source. X-ray scattering curves were obtained in three beam sessions on the Station 8.2 camera with a quadrant detector at the Synchrotron Radiation Source at Daresbury (Towns-Andrews et al., 1989; Worgan et al., 1990). A sample−detector distance of 3.26 m was used, with beam currents of 158−200 mA and a storage ring energy of 2.0 GeV. The available Q range was between 0.06 and 2.38 nm^{-1} ($Q = 4\pi(\sin\theta)/\lambda$; scattering angle = 2θ; wavelength = λ). The detector was calibrated using wet, stretched, rat tail collagen (diffraction spacing 67.0 nm). Samples of thickness 1 mm were contained in Perspex cells between mica windows of thickness 10−15 μm. Temperature control at 15 °C was achieved using a brass cell holder connected to a thermostated water bath. Sample and buffer runs lasted 10 min and were recorded as 10 time frames, in alternation with each other in the same cell in order to minimize background subtraction errors. Data were reduced using OTOKO software (P. Bendall, J. Bordas, M. H. C. Koch, and G. R. Mant, EMBL Hamburg and SERC Daresbury Laboratory, unpublished software). After normalization based on the ion chamber monitor positioned between the sample and the detector, the buffer background was subtracted from the sample run. The resulting curve was normalized using the detector response measured using a uniform ^{55}Fe radioactive source.

(e) Neutron Data Collection at the Pulsed Neutron Source ISIS. Neutron scattering data were obtained in two beam sessions on the LOQ scattering instrument at the pulsed neutron source ISIS at the Rutherford Appleton Laboratory, Didcot, U.K. (Heenan & King, 1993). The moderated pulsed neutron beam was derived from a tantalum or depleted uranium target after proton bombardment at 50 Hz (proton beam currents of 110 and 90 μA, respectively). Neutron

scattering patterns were recorded at a fixed sample-to-detector distance of 4.3 m, using a ^{3}He ORDELA wire detector. Samples and buffers were measured in 2-mm-thick rectangular quartz Hellma cells in a thermostated rack at 15 °C. Data acquisitions for (2.0−4.0) × 10^6 monitor counts took 40−65 min each for protein concentrations between 4 and 16 mg/mL. Intensities were normalized relative to the scattering from a standard calibrated partially deuterated polystyrene sample (Wignall & Bates, 1987). All sample, buffer, standard polymer, and empty beam transmissions were recorded for 5−9 min per run. The raw data were reduced using COLETTE (Heenan et al., 1989), where intensities were binned into individual diffraction patterns, based on wavelengths of 0.22−1.00 nm, and corrected for a linear wavelength dependence of the transmission measurements. The patterns were merged to give the full scattering curve in an available Q range between 0.05 and 2.2 nm^{-1}. The Q range was set in 0.04% logarithmic increments, which was optimal both for Guinier R_G and $I(0)$ analyses at low Q and for better signal-to-noise ratios at large Q.

(f) Analysis of Reduced X-ray and Neutron Data. In a given solute−solvent contrast, the radius of gyration R_G is a measure of structural elongation if the internal inhomogeneity of scattering densities can be neglected. Analyses at small Q in Guinier plots give the R_G and the forward scattering at zero scattering angle $I(0)$ (Glatter & Kratky, 1982):

$$\ln I(Q) = \ln I(0) - R_G^2 Q^2/3$$

The $I(0)/c$ values (c = sample concentration) yield molecular weights M_r (Kratky, 1963). Traditionally immunoglobulins are considered to be elongated, and in that case the radius of gyration of the cross-sectional structure R_{XS} and the cross-sectional intensity at zero angle $[I(Q).Q]_{Q\to 0}$ are obtained from (Pilz et al., 1973):

$$\ln[[I(Q)](Q)] = \ln[[I(Q)](Q)]_{Q\to 0} - R_{XS}^2 Q^2/2$$

In application to IgE-Fc, this structure is not sufficiently elongated for this analysis to be rigorous, as an axial ratio of at least 1:1:2 is required (Pilz, 1973; Hjelm, 1985). In this study, the R_{XS} analyses are used only as a monitor of curve fits. X-ray and neutron Guinier analyses were processed using the programs SCTPL4 and SCTPL5 (A. J. Beavil, A. S. Nealis, and S. J. Perkins, unpublished software). Results were collated using spreadsheets in Microsoft Excel and curve fits in Jandel Sigmaplot.

Indirect transformation of the scattering data in reciprocal space $I(Q)$ into that in real space $P(r)$ was carried out using the ITP-91 program of Glatter (Glatter & Kratky, 1982) and the GNOM program of Svergun et al. (1988), Semenyuk and Svergun (1991), and Svergun (1992).

$$P(r) = \frac{1}{2\pi^2}\int_0^\infty [I(Q)](Qr)\sin(Qr)\,dQ$$

$P(r)$ corresponds to the distribution of distances r between volume elements. This offers an alternative calculation of R_G and $I(0)$ and also gives the maximum dimension L. The X-ray $I(Q)$ curve contained 429 data points extending out to 2.15 nm^{-1}. For ITP-91, this was fitted with 8 splines with D_{max} set as 14 nm. For IgE-Fc, the neutron $I(Q)$ curve contained 58 data points extending out to 1.74 nm^{-1} and was fitted with 8 splines with D_{max} set as 14 nm. $P(r)$ was defined by 101 points. Criteria for the correct choice of splines and Lagrandian parameters for $P(r)$ were as follows: (i) $P(r)$ should exhibit positive values; (ii) the R_G from ITP should agree with the R_G from Guinier analyses; (iii) $P(r)$ should be zero when r is zero; (iv) $P(r)$ should be stable and reproducible for different experimental $I(Q)$ curves when the number of splines and D_{max} is varied over a reasonable range. L was determined from $P(r)$ when this became zero at large r; however, errors in L can be significant as a result of the low intensity of $P(r)$ in this region. For GNOM, a regularization procedure is used with an automatic choice of the transformation parameter α to stabilize the $P(r)$ calculation (Svergun, 1992). The $P(r)$ curve contain 61 points. A range of D_{max} values was tested. The final choice of D_{max} was based on the criteria (i) and (ii) above for ITP-91, and also (v) the stability of the $P(r)$ curve as D_{max} was increased beyond the estimated macromolecular length.

(g) Automated Procedure For Debye Sphere Modeling of IgE-Fc. Modeling of the X-ray and neutron scattering curves used small spheres of uniform density to represent the protein structure and the Debye equation as adapted to spheres to calculate the scattering curve (Perkins & Weiss, 1983):

$$I(Q) = \sum I_j(Q) + 2\sum\sum F_j(Q)F_k(Q)\,(\sin Qr_{jk})/Qr_{jk}$$

for N spheres of form factor $F(Q)$ and with j, k = 1 to N and $j \neq k$ in which all the distances r from each sphere to the remaining spheres are computed. The method has been tested and calibrated with known crystal coordinates (Smith et al., 1990; Perkins et al., 1993). Predicted models for IgE-Fc exist in the Brookhaven Databank (Padlan & Davies, 1986: Brookhaven reference 1IGE; Helm et al., 1991: reference 2IGE). The α-carbon coordinates formed the starting point for modeling the IgE-Fc scattering data. Models were constructed using INSIGHT II (Biosym Technologies Inc.) on Silicon Graphics Indigo Workstations (R4000 series). Two oligosaccharide chains were modeled on the complex-type sugar $Gal_2Man_3GlcNAc_4$ found in the crystal structure of human IgG-Fc at Asn297 (Deisenhofer, 1981).

The scattering curve was calculated (Figure 2) by converting the α-carbon coordinates of the IgE-Fc model to spheres using a program BRKTOS. The α-carbon coordinates were placed within a three-dimensional grid of cubes of side 0.658 nm. A cube was included for the sphere model if it contained sufficient α-carbon coordinates above a cutoff value such that the total volume of the cubes equaled that of the dry protein and carbohydrate volume calculated from the sequence (Table 2; Chothia, 1975; Perkins, 1986). A total of 371 cubes were used for IgE-Fc. For X-ray modeling, the dry volumes were increased to allow for a hydration shell, assumed to comprise 0.3 g of water/g of glycoprotein and an electrostricted volume of 0.0245 nm^3 per bound water molecule (Perkins, 1986). This volume increase was used to rescale the cube coordinates, and their side became 0.730 nm. The Debye simulations using the program SCT were based on overlapping spheres with radii of 0.453 nm placed at the center of each cube with the same total volume as the cubes. This is much less than the nominal resolution of $2\pi/Q_{max}$ of the scattering curves, which is 2.8 nm for Q_{max} = 2.24 nm^{-1} in this study. No corrections were applied for X-ray wavelength spread or beam divergence as these are

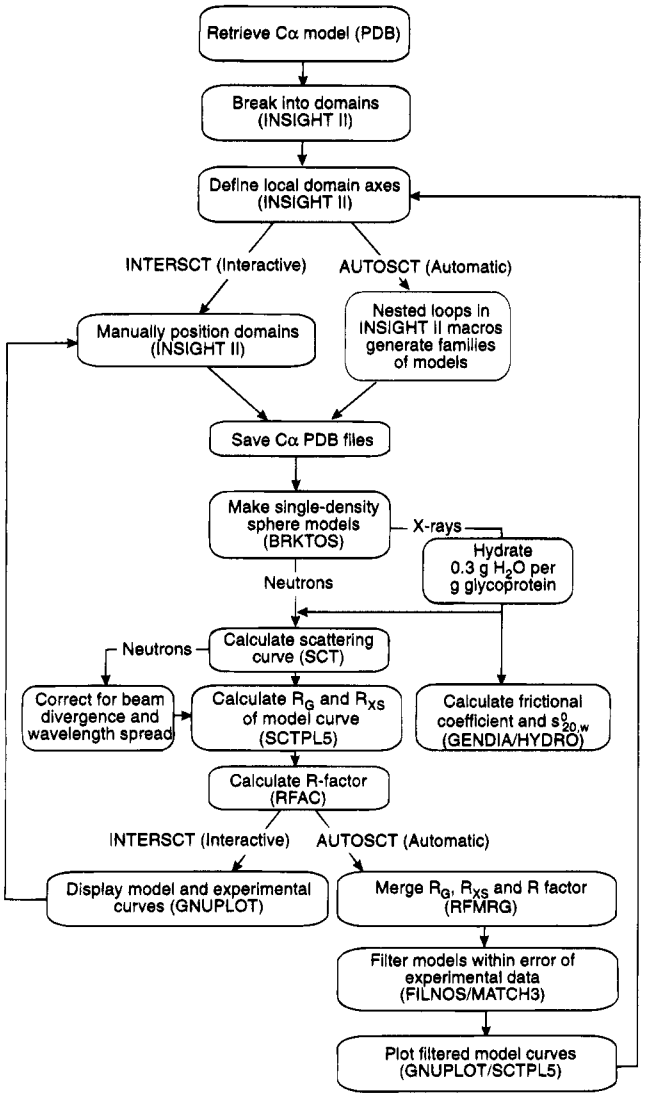

FIGURE 2: Flow diagram of the stages involved in the INTERSCT and AUTOSCT modeling procedures. Each box describes a calculation and the program used for it. The automation of both procedures is achieved by the use of INSIGHT II and UNIX executable script files.

thought to be negligible. A 16% wavelength spread for a nominal λ of 1.0 nm and a beam divergence of 0.016 radians were used to correct the calculated neutron scattering curve for the reasons discussed in Mayans et al. (1995).

The display and curve fitting program SCTPL5 was used to assess the models. R_G and R_{XS} values were determined from the calculated curves in the same Q ranges that had been used to fit the experimental data. A goodness-of-fit R factor, $R = 100 \times \Sigma|I(Q)_{exp} - I(Q)_{cal})|/\Sigma|I(Q)_{exp}|$, was computed using RFAC by analogy with the crystallographic R factor (Smith et al., 1990). Note that R will depend on the Q range in use and the number of data points in that Q range and should be normalized against $I(Q)_{cal}$ for a given curve fitting exercise. R was used initially with the Q range out to 0.5 nm^{-1} to determine the scaling factor to match the experimental and calculated $I(Q)$ curves, for which $I(0)_{cal}$ was set as 1000 in order to define a working scale for curve comparisons. This encompasses the Q ranges used for R_G and R_{XS} determinations. To determine the quality of curve fits, R was then computed for successive Q ranges from 0.13 nm^{-1} out to 0.8–2.0 nm^{-1} in 0.2 nm^{-1} steps (denoted $R_{0.8}$ to $R_{2.0}$). R factors are not comparable between different curve fitting exercises and are primarily influenced by the large $I(Q)$ values at low Q.

The above programs were linked to provide an interactive (INTERSCT) and an automated (AUTOSCT) curve fitting procedure (Figure 2). Full domain models were generated using INSIGHT II from the atomic structures for individual domains. Domains were constrained in space by their known structures and reasonable stereochemical links between them. IgE-Fc was considered as four independently-movable fragments, namely, the domain pairs $(C\epsilon2)_2$ and $(C\epsilon4)_2$ and the two individual Cε3 domains with their associated carbohydrate chain (Figure 1). The residue numbering is 229–329 for the Cε2 domain, 330–438 for the Cε3 domain, and 439–547 for the Cε4 domains in the scheme of Table 1 in Padlan and Davies (1986). Breaks between the domains were chosen to give convenient local rotation axes. The center of rotation of the $(C\epsilon2)_2$ domain pair was set as a pseudoatom defined as the geometric center of the α-carbons of Asp330 in the two chains A and B; its x-axis was defined both by this pseudoatom and a second pseudoatom at the geometrical center of the $(C\epsilon2)_2$ domain pair; the xy plane was defined by the addition of the α-carbon of Asp330A. The center of rotation of the $(C\epsilon4)_2$ domain pair was set as the α-carbon of Pro439B, its x-axis was defined by the addition of the α-carbon of Pro439A, and the xy plane was defined by the further addition of the α-carbon of Lys547A. The center of rotation of one Cε3 domain was set as the α-carbon of Pro439A, its x-axis was defined by the addition of the α-carbon of Pro439B, and the xy plane was defined by the further addition of the α-carbon atom of Gly438A. For the other Cε3 domain, the equivalent atoms were those of residues Pro439B, Pro439A, and Gly438B in that order.

In both INTERSCT and AUTOSCT, INSIGHT II macros triggered UNIX shell scripts to generate coordinate models (Figure 2) from which a scattering curve was calculated for comparison with experimental data.

(i) INTERSCT permitted the interactive manipulation of the separate domains. Any coordinate model was transformed into a curve fit within 10–20 s in a separate window using GNUPLOT. INTERSCT was useful for exploring the effect of possible domain conformation on curve fits, and for defining sets of domain structures that could be submitted for more extensive searching. Each new domain position relative to its starting position was determined by calculation of the superposition matrix required to move the new position back to its starting position.

(ii) AUTOSCT used INSIGHT II macros to explore two or more degrees of rotational and/or translational freedom between the independent domains. The axes of the independent domains were driven in a concerted stepwise manner by a series of nested loops within the macro scripts to generate many hundreds of models. Scattering curves were calculated and analyzed (Figure 2) to generate a list of the geometrical steps used to define the model, the R_G and R_{XS}, and $R_{0.8}$ to $R_{2.0}$. The list was sorted using the R factor to filter out the best models for further investigation. AUTOSCT was useful for the exhaustive exploration of domain movements and permitted the precision of the best-fit domain model to be determined.

(iii) The same procedure can be used to assess frictional coefficients f calculated from experimental sedimentation coefficients $s^0_{20,w}$. The hydrated X-ray scattering model (but

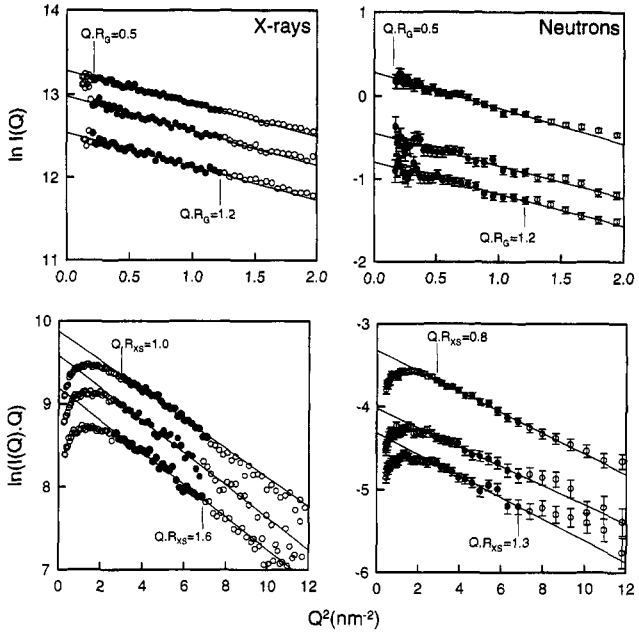

FIGURE 3: Guinier R_G and R_{XS} plots for recombinant IgE-Fc. Dilution series of IgE-Fc at concentrations of 12.2, 9.2, and 6.1 mg/mL (X-rays) and 14.3, 7.2, and 5.5 mg/mL (neutrons) are shown. The filled circles between the QR_G and QR_{XS} ranges as arrowed show the data points used to determine R_G and R_{XS} values; these are otherwise denoted by open circles. The Q ranges used for R_G and R_{XS} fits are 0.14−0.35 and 0.52−0.83 nm^{-1}, respectively. Statistical error bars in the neutron data are shown when these are large enough to be visible.

using nonoverlapping spheres to satisfy the algorithm in use) can be directly used to calculate f values, using the modified Oseen tensor procedure in the program GENDIA (Garcia de la Torre & Bloomfield, 1977a,b; Perkins et al., 1993). The more recent hydrodynamic modeling program HYDRO which permits overlapping spheres (Garcia de la Torre, 1989) gives results that were very similar to those from GENDIA.

RESULTS AND DISCUSSION

(a) Synchrotron X-ray Scattering Data on IgE-Fc. Recombinant human IgE-Fc was studied using X-ray scattering to identify the overall solution structure of its six domains (Figure 1). Scattering data were analyzed in two Q ranges in order to obtain the R_G and R_{XS} values. Figure 3 shows that linear plots in satisfactory QR_G and QR_{XS} ranges were obtained, although the R_{XS} data were only approximate (Materials and Methods). Time-frame analyses showed pronounced radiation damage effects through apparent aggregate formation which caused both the R_G and $I(0)$ values at low Q to rise with time of irradiation after a small lag period of 1 min. These were not observed for the R_{XS} and $[[I(Q)](Q)]_{Q\to 0}$ analyses in a larger Q range. Between 4 and 7 min of irradiation, the rate of increase in $I(0)$ and R_G appeared to be linear as a function of irradiation time. Interestingly, these rates were directly proportional to sample concentration. It was not possible to use linear or quadratic extrapolation schemes to zero irradiation time. Accordingly, here and below, all data analyses were based on the use of the first 1 min time frame alone in 10 min data acquisitions. Dilution series between 3.0 and 12.2 mg/mL showed no concentration dependence of the Guinier R_G or $I(0)/c$ parameters (c: sample concentration).

Table 1 shows that the X-ray R_G value of IgE-Fc is 3.52

Table 1: Guinier and $P(r)$ Analyses of Human IgE-Fc[a]

	R_G (nm)	R_{XS} (nm)	L (nm)
	X-ray Scattering		
Guinier	3.52 ± 0.14 (6)	1.89 ± 0.05 (8)	
ITP-91	3.58 ± 0.12 (6)		13 ± 0.5
GNOM	3.64 ± 0.15 (6)		13 ± 0.5
	Neutron Scattering (^2H_2O Buffer)		
Guinier	3.53 ± 0.05 (6)	1.56 ± 0.09 (6)	
ITP-91	3.65 ± 0.12 (6)		13 ± 1
GNOM	3.70 ± 0.08 (6)		13

[a] The Guinier R_G and R_{XS} values are the mean ± standard deviation of a total of separate measurements as bracketed. The Q range used for fitting and the concentration range are specified in Figure 3. The ITP-91 and GNOM $P(r)$ calculations of R_G and L values are summarized, where L corresponds to the longest dimension of the macromolecule. The neutron determination of L by ITP-91 and GNOM for IgE-Fc correspond to the maximum dimension assumed in the $P(r)$ calculation.

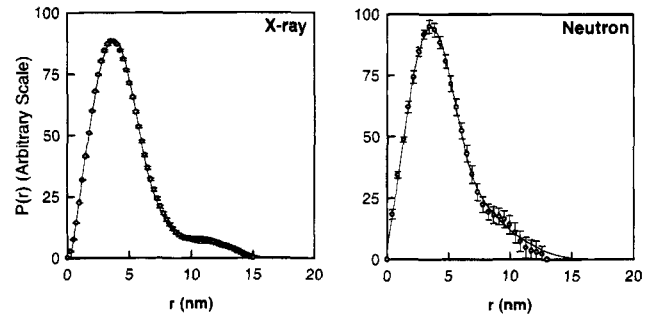

FIGURE 4: Distance distribution functions $P(r)$ for IgE-Fc. $I(Q)$ data were processed to give $P(r)$ using ITP-91 (line) and GNOM (circles). The X-ray $P(r)$ curve corresponds to 6.3 mg/mL IgE-Fc. The neutron $P(r)$ curve corresponds to 14.6 mg/mL IgE-Fc. Statistical error bars from GNOM are shown when these are large enough to be visible.

nm (which is an upper limit for reason of radiation effects), and its R_{XS} value is 1.89 nm. The R_G/R_O ratio indicates the anisotropy or degree of elongation of the structure, where R_O is the R_G of the sphere with the same volume as the protein. The value of R_G/R_O is 1.46 ± 0.07, which is slightly higher than the value of 1.28 ± 0.10 typically found for globular proteins (Perkins, 1988). This is suggestive that the 6 domains of IgE-Fc are in a more extended arrangement than in a single-domain globular protein of the same volume.

Calculation of the X-ray $P(r)$ (Figure 4) was carried out using both ITP-91 and GNOM with the $I(Q)$ curve from the first minute of data acquisition. This widely-used method leads to an alternative determination of R_G and L. The two algorithms gave R_G values of 3.58 and 3.64 nm, a $P(r)$ maximum at 3.6 ± 0.1 and 3.7 ± 0.1 nm, and a maximum dimension L of 13 nm. The $I(Q)$ curve transformations to $P(r)$ were not completely stable in a range of assumed maximum dimensions from 9 to 15 nm. Nonetheless, the Guinier R_G and $I(0)$ parameters were in good agreement with those calculated from $P(r)$ (Table 1), indicating the self-consistency of the data analyses. Little difference was seen between ITP-91 and GNOM (Figure 4).

(b) Neutron Scattering Data on IgE-Fc. Neutron scattering data were also obtained for IgE-Fc in 100% ^2H_2O buffers. These complement the X-ray data by providing a control of X-ray radiation damage effects, possible internal scattering density inhomogeneity effects, and molecular weights. The Guinier analyses of Figure 3 show that linear R_G and R_{XS} plots were obtained. Trace IgE-Fc sample aggregation was

observed at the lowest Q values in the $I(Q)$ curves at Q values in a range less than that used for the X-ray Guinier fits (Table 1). This is the likely consequence of the effect of ^2H_2O buffers which can promote protein aggregation. From a concentration series between 3.6 and 14.3 mg/mL, the neutron R_G of IgE-Fc was determined to be 3.53 nm as an upper limit in good agreement with the X-ray value, showing that X-ray radiation effects on IgE-Fc have at least been mostly eliminated. The R_{XS} value of IgE-Fc was 1.56 nm. This is slightly smaller than the corresponding X-ray value of 1.89 nm, and the effect of this is visible in the Guinier plots of Figure 3. This may result from scattering density inhomogeneity, when surface carbohydrate and hydrophilic amino acids will contribute more strongly than hydrophobic amino acids to the X-ray scattering curve, but less strongly to the neutron scattering curve in 100% ^2H_2O (Perkins, 1986, 1988). Comparison of $I(0)/c$ for IgE-Fc (of known sequence: Young et al., 1995) with those measured for other proteins on LOQ [bovine IgG1 and IgG2 (Mayans et al., 1995); human tissue factor and factor VIIa (Ashton et al., 1995); molecular weights from 25 000 to 144 000], all relative to a polystyrene standard (Wignall & Bates, 1987), showed that IgE-Fc had a molecular weight of 86 000 ± 12 000. While this is slightly higher but within error of the value of 75 300 calculated from its sequence and assumed carbohydrate composition, it shows that the X-ray and neutron analyses correspond to a monomeric IgE-Fc structure.

Calculation of the distance distribution functions $P(r)$ was carried out using both ITP-91 and GNOM (Figure 4). The use of GNOM gave similar R_G and L values to those derived from the X-ray data (Table 1). A $P(r)$ maximum of 3.6 ± 0.1 and 3.5 ± 0.2 nm was determined using GNOM and ITP-91, respectively. As for the X-ray data, an upper limit on the value of L was determined to be 13 nm from the neutron $P(r)$ curves.

(c) INTERSCT Scattering Curve Modeling of IgE-Fc. Curve modeling was used in order to determine the arrangements of the Cε2, Cε3, and Cε4 domains in IgE-Fc that best accounted for the experimental X-ray and neutron curves, using a tested curve fitting procedure. Models were initially assessed by the manual INTERSCT procedure (Figure 2). The experimental X-ray curve at the highest concentration of 12.2 mg/mL IgE-Fc was compared with curves calculated from the Brookhaven Protein Data Bank IgE-Fc models 1IGE (Padlan & Davies, 1986) and 2IGE (Helm et al., 1991). Figure 5a shows that both models gave poor curve fits, although the R_G and R factor values show that 1IGE gave a significantly better fit than 2IGE (Table 2). In the 1IGE and 2IGE models, the Cε3 and Cε4 domains are modeled identically on the basis of the IgG-Fc crystal structure (Deisenhofer, 1981), but differ in their Cε2 domains and the connection between the Cε2 and Cε3 domains. The 2IGE model contains a remodeled Cε2 domain and a longer linker between the Cε2 and Cε3 domains following correction of the disulfide bridge linkages between the Cε2 chains to that shown in Figure 1. The 2IGE model is thus more elongated than the 1IGE model, and this is reflected in its larger R_G value.

Given the good sequence similarity between the Cε3 and Cε4 domains in IgE-Fc and the Cγ2 and Cγ3 domains in IgG-Fc (Padlan & Davies, 1986), the most likely uncertainty in the IgE-Fc model is the location of the Cε2 domain pair.

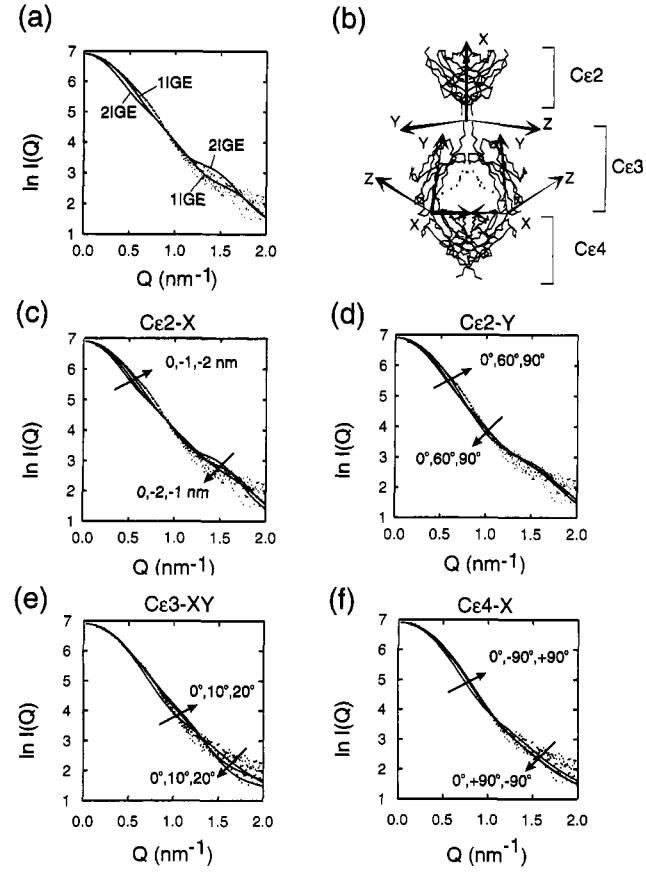

FIGURE 5: INTERSCT comparisons of the experimental X-ray scattering curve of IgE-Fc with various domain models for IgE-Fc. (a) 1IGE and 2IGE are the IgE-Fc models from the Brookhaven Database. 1IGE has a compact linear structure, while 2IGE is a more extended linear model which incorporates the correct inter-heavy chain disulfide bridge pairing (Figure 1). (b) The 2IGE model is redefined in terms of local domain axes for the Cε2 domain pair and the two Cε3 domains. The x-axis of the Cε4 domains is coincident with the x-axis of their neighboring Cε3 domains. The taperings of the axes indicate their directions. (c) 2IGE models in which the Cε2 domain pair is translated by 0, −1, and −2 nm along its x-axis shown in (b) to generate compact structures. Here and in (d), (e), and (f), the numbered arrows identify the curve simulations in question. (d) 2IGE models in which the Cε2 domain pair is translated by −1 nm along its x-axis, and rotated about its y-axis by 0°, 60°, and 90° to generate bent, compact structures. (e) 2IGE models in which the Cε2 domain pair is translated by −1 nm along its x-axis and rotated about its y-axis by 90°, and both Cε3 domains are rotated by 0°, 10°, and 20° about both their x- and y-axes. (f) 2IGE models in which the Cε2 domain pair is translated by −1 nm along its x-axis and rotated about its y-axis by 90°, and the Cε4 domain pair is rotated by 0°, −90°, and +90° about its x-axis. The −90° model gives an S-shaped model, while the +90° model gives a U-shaped model.

Since the 2IGE model contains the correctly disulfide bonded Cε2 domain, this was used as a starting point for subsequent model fitting. The precise interaction between the Cε2 domains in the pair is not known (Helm et al., 1991). This 2IGE structure was divided into four independently movable segments, namely, the Cε2 domain pair, two independent Cε3 domains, and the Cε4 domain pair (Materials and Methods). Figure 5b defines the axes involved in manual INTERSCT rotations and translations of the Cε2 domain pair relative to the Cε3 and Cε4 domains. From this, it can be seen that the coupling of rotations about both the Cε2 x-axis and y-axis covers all the possible orientations of the Cε2 domain pair relative to the Cε3 domains. Figure 5c shows

Table 2: INTERSCT Curve Fit Analyses for the IgE-Fc Models Depicted in Figure 5

	model	Cε2 x-axis translation (nm)	Cε2 y-axis rotation (deg)	Cε3−Cε4 domain rotations (deg)	R_G (nm)	R_{XS} (nm)	$R_{1.0}$	$R_{2.0}$
Figure 5a	1IGE	0	0		3.6	1.9	6.1	6.5
	2IGE	0	0		4.1	1.5	10.9	11.8
Figure 5c	2IGE	0	0		4.1	1.5	10.9	11.8
	2IGE	−1	0		3.8	1.8	8.4	8.9
	2IGE	−2	0		3.5	2.0	5.1	5.7
Figure 5d	2IGE	−1	0		3.8	1.8	8.6	8.9
	2IGE	−1	60		3.6	2.0	7.1	7.5
	2IGE	−1	90		3.3	2.2	4.7	5.1
Figure 5e	2IGE	−1	90	Cε3, x-axis, 0, y-axis, 0	3.4	2.1	4.5	5.0
	2IGE	−1	90	Cε3, x-axis, 10, y-axis, −10	3.3	1.9	2.4	3.3
	2IGE	−1	90	Cε3, x-axis, 20, y-axis, −20	3.3	1.8	2.5	3.8
Figure 5f	2IGE	−1	90	Cε4, x-axis, 0	3.4	2.1	4.5	5.0
	2IGE	−1	90	Cε4, x-axis, +90	3.1	1.9	3.3	4.1
	2IGE	−1	90	Cε4, x-axis, −90	3.2	2.0	3.0	3.6

that an x-axis translation of the Cε2 domain pair toward the Cε3 and Cε4 domains improves the fit with experiment such that the model becomes equivalent to 1IGE (Table 2). The application of a rotation of the Cε2 domain pair about its y-axis to one of the models of Figure 5c to generate a bent model further improves the curve fit as shown in Figure 5d. Such a y-axis rotation of 90° offered better curve fits with lower $R_{1.0}$ and $R_{2.0}$ values (where $R_{1.0}$ and $R_{2.0}$ correspond respectively to the R factors extending to $Q = 1.0$ and 2.0 nm^{-1}) than 1IGE, although the R_G of this model is now too low. However, these rotational and translational searches and their combinations showed that no good curve fit could be achieved by a suitable adjustment of the Cε2 domain pair alone. All the simulations underestimated the observed intensities between Q values of 0.5−1.0 nm^{-1}.

Improved curve fits were obtained by further manual INTERSCT searches of the IgE-Fc model. These were now based on independent movements of the Cε3 and Cε4 domains. In Figure 5e, starting from the best model from Figure 5d, small rotations were applied about both the Cε3 x-axis and y-axis simultaneously. This has the effect of making the domains cross over each other more tightly. While the R_G and R_{XS} values remained acceptable, the $R_{1.0}$ and $R_{2.0}$ values and the curve fit in Figure 5e out to Q of 1 nm^{-1} were significantly improved. At large Q, the curve fit was not improved. In Figure 5f, the effect of applying large positive or negative rotations of the Cε4 domain pair about its x-axis was explored. Rotations of ±90° applied to the best model from Figure 5d resulted in clearly better curve fits, but not as good as those in Figure 5e (Table 2). In both cases, some steric overlap was detected between the domains. In summary, the manual approach was used for testing the effects of domain movements on curve fits, and for defining sets of domain movements for more extensive study by AUTOSCT (below). It can however lead to problems with steric overlap between domains. Nonetheless, Figure 5 shows that the scattering curves are sensitive to the relative positions of the domains in IgE-Fc and that they can be used to assess the IgE-Fc structure.

(d) AUTOSCT Systematic Searches of IgE-Fc Structures. An extensive automated survey of IgE-Fc model comparisons with the experimental X-ray curve was now carried out using the AUTOSCT procedure. Five domain rotations and translations were explored simultaneously, using nested loops within the macro script files to generate thousands of models to ensure that all reasonable structures have been checked. In terms of the curve fits, the effects of domain movements were not independent of one other. This ruled out a stepwise approach in which each domain movement is optimized one by one, as in Figure 5. From this analysis, the precision of the final model can be determined from the range of structures that are permitted by the precision of the experimental data.

Table 3 first summarized the five domain movements that were used to search four types of possible structures for IgE-Fc, which were based on Figure 5. The complete range of steps defined in Table 3 produced 4 × 5 × 9 × 13 × 4 = 9360 models. It is important to note that the order of the rotations and translations is noncommutative. For the searches that correspond to those explored manually in Figure 5e, the starting model was that of 2IGE, adapted by a 10° x-axis and a −10° y-axis rotation on each Cε3 domain. For those corresponding to the Figure 5f searches, the starting model was that of 2IGE itself. As the location of the Cε2 domain pair is the least known aspect of the model, its position was searched in the greatest detail.

The four searches were implemented according to the following sequence of domain movements (Table 3):

(i) The Cε4 x-axis rotation of the lower part of the IgE-Fc structure (Figure 5b) in positive and negative directions produced two ranges of IgE-Fc structures which are bent at the Cε3−Cε4 linker region. These two ranges of structures overlapped in the region where the Cε4 x-axis rotation is 0°. Together with the rotations described in (iv) below, this produced the U-shaped and S-shaped IgE-Fc structures for each of the families of models corresponding to the manual searches shown in Figure 5e and 5f.

(ii) In all four searches, the negative Cε2 x-axis translations moved the Cε2 domain pair toward the Cε3/Cε4 domains to generate a series of increasingly more compact structures.

(iii) In all four searches, the Cε2 x-axis rotations corresponded to rotating this domain pair about its vertical axis. The stepping was initiated by a +90° rotation about the Cε2 x-axis, then rotating the Cε2 domain back in −20° steps through the full range of 180°. The position corresponding to the starting 2IGE model is 0° in Table 3.

(iv) The Cε2 y-axis rotations of the upper part of the IgE-Fc structure (Figure 5b) now generated the bent IgE-Fc models of interest. In combination with the negative x-axis rotations of the Cε4 domains in (i) above, this yielded the U-shaped structures. Positive x-axis rotations of the Cε4 domains generated the S-shaped structures. In combination with the Cε2 x-axis rotations in (iii) above, this permitted

Table 3: AUTOSCT Data Analyses for the Best 100 S-Shaped and U-Shaped Models for the X-Ray Scattering Curve of IgE-Fc

	domain search parameters					model fitted parameters				
	Cϵ4 *x*-rot (deg)	Cϵ2 *x*-tran-1 (nm)	Cϵ2 *x*-rot (deg)	Cϵ2 *y*-rot (deg)	Cϵ2 *x*-tran-2 (nm)	R_G (nm)	R_{XS} (nm)	$R_{1.0}$	$R_{2.0}$	$s^0_{20,w}$ (S)
Experimental Values										
						3.52 ± 0.14	1.89 ± 0.05			4.7 ± 0.1
survey and evaluation of models										
range tested [steps]	0−(±90) [30]	−0.5−(−2.5) [−0.5]	90−(−70) [−20]	0−120 [10]	0.0−1.5 [0.5]					
Q range fitted (nm^{-1})						0.14−0.35	0.52−0.83	0.13−1.00	0.13−2.00	
Figure 5e Models										
Best 100 U-Shaped Models from 3296 Models Filtered from 9360										
mean	−37 ± 21	−1.4 ± 0.7	27 ± 43	84 ± 18	0.5 ± 0.4	3.2 ± 0.6	1.94 ± 0.06	2.8 ± 0.2	3.6 ± 0.2	4.76 ± 0.05
range in best models	0−(−90)	−0.5−(−2.5)	90−(−70)	40−120	0.0−1.5	3.1−3.3	1.8−2.0	2.5−3.3	3.2−3.9	4.7−4.9
observed range						2.8−4.4	0.9−2.3	2.5−11.9	3.2−14.4	3.7−5.1
Best 100 S-Shaped Models from 4923 Models Filtered from 9360										
mean	51 ± 16	−1.3 ± 0.7	28 ± 42	93 ± 17	0.6 ± 0.4	3.2 ± 0.1	1.92 ± 0.04	2.7 ± 0.1	3.4 ± 0.1	4.78 ± 0.07
range in best models	0−60	−0.5−(−2.5)	90−(−70)	50−120	0.0−1.5	3.1−3.3	1.8−2.0	2.5−3.0	3.1−3.7	4.4−4.9
observed range						2.8−4.4	0.8−2.3	2.5−11.8	3.1−14.1	3.6−5.2
Figure 5(f) Models										
Best 100 U-Shaped Models from 7250 Models Filtered from 9360										
mean	−81 ± 14	−1.8 ± 0.7	−10 ± 30	51 ± 34	0.2 ± 0.4	3.2 ± 0.5	1.96 ± 0.03	2.8 ± 0.2	3.5 ± 0.1	4.79 ± 0.12
range in best models	−60−(−90)	−0.5−(−2.5)	90−(−70)	0−110	0.0−1.5	3.1−3.3	1.9−2.0	2.6−3.2	3.3−3.8	3.8−5.1
observed range						2.8−4.5	1.0−2.5	2.6−12.6	3.3−14.2	3.6−5.7
Best 100 S-Shaped Models from 7010 Models Filtered from 9360										
mean	65 ± 12	−1.8 ± 0.8	−19 ± 35	64 ± 41	0.3 ± 0.6	3.2 ± 0.5	1.99 ± 0.03	3.0 ± 0.1	3.6 ± 0.1	4.75 ± 0.05
range in best models	60−90	−0.5−(−2.5)	90−(−70)	0−120	0.0−1.5	3.1−3.3	1.9−2.0	2.8−3.2	3.4−3.9	4.6−5.1
observed range						2.9−4.5	0.9−2.5	2.8−12.6	3.4−14.3	3.5−5.7

exploration of all the regions in the IgE-Fc model which involve bending of the Cϵ2 domain pair.

(v) In all four searches, the fifth parameter involved a second Cϵ2 *x*-axis translation in the opposite direction to the first one in (ii). This did not negate the first translation in (ii) except when the *y*-axis rotation of the Cϵ2 domains is 0°, because it was applied following the Cϵ2 *x*-axis and *y*-axis rotations. This translation was introduced to improve the IgE-Fc models with large *y*-axis rotations of the Cϵ2 domains, which can suffer from steric overlap with the Cϵ3 domains.

As the four searches of Table 3 each involved 9360 models, it was necessary to filter and assess the resulting curve fits. First, in each search, the models were filtered by eliminating all those in which there were less than 360 spheres as the results of substantial steric overlaps between the domains. The composition and volume of IgE-Fc required optimally 371 spheres (Materials and Methods). Next, all the models were assessed on the basis of their R_G, R_{XS}, $R_{1.0}$, and $R_{2.0}$ values using histograms. Before removal of overlapping spheres, histograms of the R_G and $R_{2.0}$ values as exemplified in Figure 6 showed that steric overlap of the domains had generated a large number of artifactual models with predominantly lower R_G and $R_{2.0}$ values. Their removal left 3296, 4923, 7250, and 7010 valid models from 9360 in each of the four structural searches. Table 3 and Figure 6 showed that, as expected, $R_{2.0}$ values were more effective than R_G values for selecting the best-fitting models. The $R_{2.0}$ values monitored a larger Q range, which is advantageous if the R_G data are affected by trace amounts of aggregates, and spanned a larger numerical range of values, which makes them more discriminating of good models than the R_G values. A good model fit was readily defined by the lowest R factors in the histogram (Figure 6). In contrast, the R_G values in the histogram can be larger or smaller than

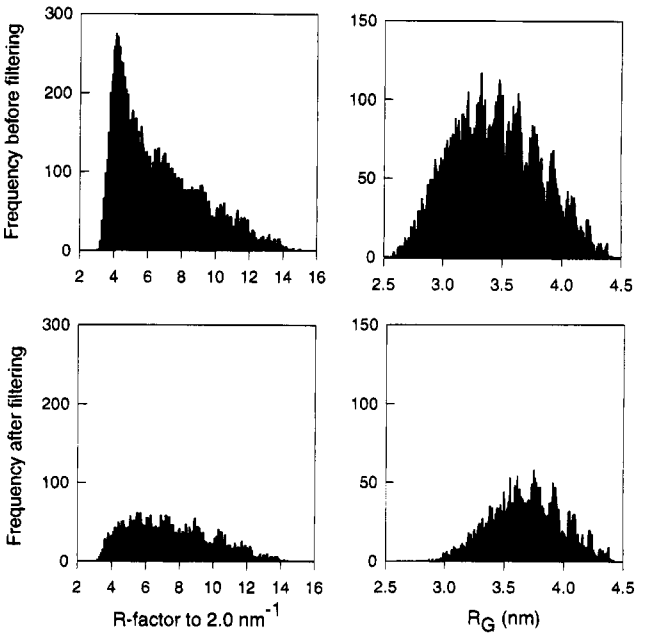

FIGURE 6: Histogram of the AUTOSCT analysis of the X-ray scattering curve for 9360 U-shaped models for IgE-Fc. The models were generated in the course of a five-parameter search based on the U-shaped models and Figure 5e, i.e., two X-axis translations of the Cϵ2 domain, two rotations about the *x*- and *y*-axis of the Cϵ2 domain, and rotation about the *x*-axis of the Cϵ4 domain. The upper and lower pairs of histograms correspond to the 9360 models before filtering for steric overlaps, and the 3296 models left after filtering.

the desired R_G value, and this raised the question of the most appropriate R_G range to use to define a good fit. The disadvantage of R factors was that their comparative usage is restricted to a single experimental curve, even though several such curves may be available (Table 1), as R factors are not presented as absolute values.

The outcome of each of the four searches of satisfactory structures was defined by taking the 100 models with the best $R_{1.4}$ values. $R_{1.4}$ values were employed in order to utilize the strongest experimental signal-to-noise ratios, although there was little difference from the use of $R_{2.0}$ values. The mean and standard deviation of the five search parameters are summarized in Table 3. Similar results were obtained if the 400 best models in each set were used. This indicated that the top 100 models were a representative sample. Different pairs of search parameters were examined to show that large numbers of sterically-possible IgE-Fc models had been eliminated. This showed that the method was sufficiently discriminatory to result in a limited family of IgE-Fc structures.

The final structures were different for the searches derived from each of Figures 5e and 5f, and these will now be summarized in turn:

(i) For the two Figure 5e searches, the principal effect of the small ±10° *x*/*y*-axes rotation of the Cε3 domains applied to the 2IGE starting model is that the Cε2 domain pair must be rotated by at least 40°, and by an average of 84 ± 18° or 93 ± 17°, about its *y*-axis to generate a bent IgE-Fc structure in the U-shaped and S-shaped sets of models (Table 3). No good fit existed when this Cε2 rotation was less than 40−50°. This Cε2 *y*-axis rotation was correlated with a vertical Cε2 *x*-axis translation such that an increased *y*-axis bending of the Cε2 domains is associated with a reduced translation along its *x*-axis toward the Cε3/Cε4 domains. The Cε2 domain pair was rotated by an average of 27 ± 43° about its *x*-axis in both searches. This was within error of its starting value of 0° in the 2IGE model; any value between −90° and 70° was available to the model as the scattering curve was not sensitive to this rotation. The Cε4 domain pair was rotated by an average of −37 ± 21° or by 51 ± 16° about its *x*-axis in the U-shaped or S-shaped structures, but the ranges found for the best 100 models do include 0° (Table 3). Thus while IgE-Fc *must* be bent about the Cε2−Cε3 junction, the range of solutions summarized in Table 3 show that those with no Cε3−Cε4 bends are also permitted.

(ii) For the two Figure 5f searches, if no *x*/*y*-axes rotations of the Cε3 domains were applied to the starting 2IGE model, the principal result was that the bending of Cε4 about its *x*-axis by an average of −81 ± 14° or 65 ± 12° was a requirement for obtaining a good curve fit. Only *x*-axis rotations of ±60−90° in the Cε4 domain were found in the 100 best models. In these models, the Cε2 domains were rotated by an average of 51 ± 34° and 64 ± 41° for the U- and S-shaped models, respectively, but the ranges observed include 0° (Table 3). Thus, in this set of models, the complementary result was obtained that IgE-Fc *must* be bent by a considerable amount at the Cε3−Cε4 junction, but models with no bend at the Cε2−Cε3 junction were permitted.

The mean and standard deviation of the R_G, R_{XS}, $R_{1.0}$, and $R_{2.0}$ parameters are summarized in Table 3 for each of the four sets of 100 best-fit models. The mean R_G values in the 100 best models (3.2 ± 0.6 nm) were slightly less than the experimentally observed R_G values (3.52 ± 0.14 nm). This difference was attributed to the effect of trace aggregation that occurred during the first minute of X-ray data acquisition which would increase the observed R_G value. Models with a larger R_G value that agreed with the observed R_G value gave worsened *R* factors and curve fits. The mean R_{XS} values

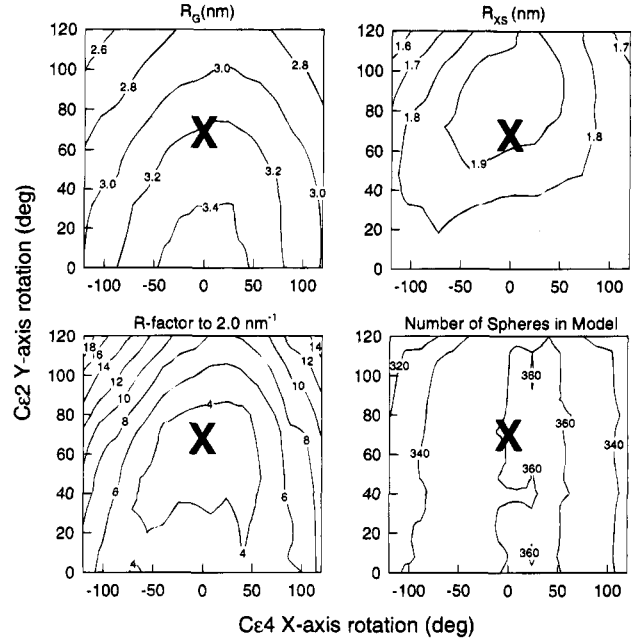

FIGURE 7: Contour maps of a two-parameter AUTOSCT search for IgE-Fc models. These were generated from a 2IGE model to which a first translation of the Cε2 domain by −0.5 nm on its *x*-axis, an *x*-axis rotation of 0°, and a second *x*-axis translation of 0.5 nm have been applied. The *y*-axis rotation of the Cε2 domain is scanned with the *x*-axis rotation of the Cε4 domain. This assesses a series of IgE-Fc models of different bends between the Cε2 and Cε3 domains, and the Cε3 and Cε4 domains. Contour maps are shown for the calculated R_G and R_{XS} parameters of the ensuing models, together with the *R* factor out to 2.0 nm^{-1} and the total number of spheres in the IgE-Fc model (to monitor steric overlap between domains). The cross indicates the location of the model used in Figure 8.

in the 100 best models (1.95 ± 0.06 nm) agreed well with the observed value (1.89 ± 0.05 nm). The $R_{1.0}$ and $R_{2.0}$ values were good at 2.5−3.3% and 3.1−3.9% in all four sets of the 100 best models, showing that the scattering data are not able to distinguish between these four different types of IgE-Fc structures. Comparable curve fits were obtained with the other X-ray curves measured at lower concentrations (3.0−9.2 mg/mL IgE-Fc), although the *R* factors were poorer due to the lower experimental signal-to-noise ratios. In conclusion, the analyses of 37 440 models show that the structure of IgE-Fc as determined by scattering is bent at either the Cε2−Cε3 junction, or the Cε3−Cε4 junction, or both, and that planar IgE-Fc structures are ruled out.

Several series of 2D contour maps were generated to summarize the range of allowed models that involve bending between the Cε2−Cε3 and the Cε3−Cε4 domains. The purpose of these maps was to confirm that no further improvement to the curve fits could be obtained and permit an estimate of the error range of the final models. The maps in Figure 7 were derived from the best curve fits when the Cε3−Cε4 junction is not bent, as such a bend is less likely to occur (see Conclusions). The mean values of the two Cε2 *x*-axis translations were fixed at −2.0 and 0.0 nm, and the mean *x*-axis rotation was fixed at 30°. These contour plots demonstrated a single minimum for the *R* factor at a Cε2 *y*-axis rotation of 70° and a Cε4 *x*-axis rotation of 0°, and good agreement with the three parameters (R_G, R_{XS}, and the total of spheres). An IgE-Fc structure with this Cε2 *y*-axis and Cε4 *x*-axis rotation was used to give the excellent X-ray curve fit of Figure 8 with an $R_{2.0}$ of 3.4%. The R_G of

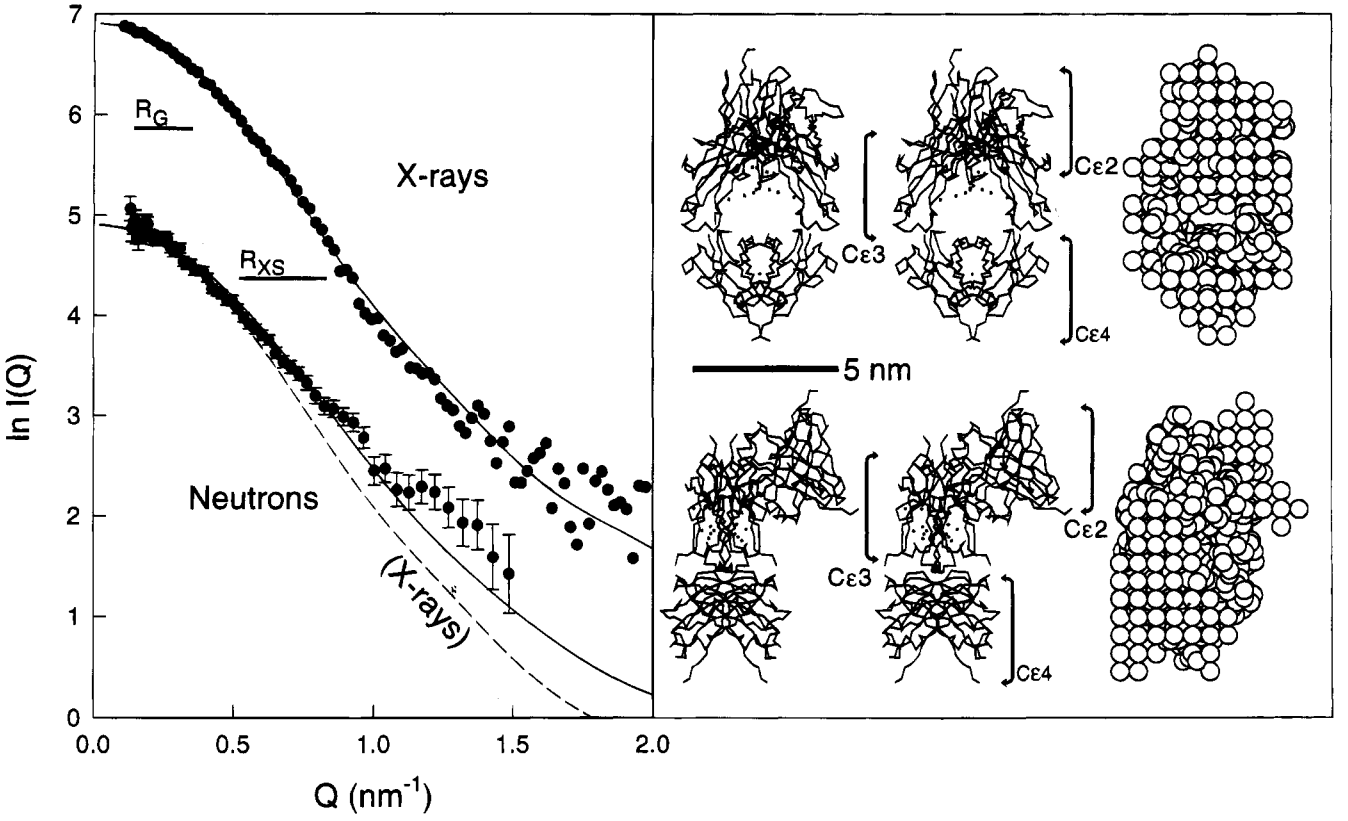

FIGURE 8: Comparisons of a typical curve simulation based on one of the best-fit IgE-Fc models with the experimental X-ray and neutron scattering curves. The 2IGE model is taken from that of Figure 5e with rotations of 10° and −10° of the Cε3 domains about their *x*- and *y*-axes, respectively. The X-ray scattering curve fit has an *R* factor of 3.3% out to *Q* of 2.0 nm^{-1}, based on a curve measured at 12.2 mg/mL IgE-Fc. The neutron scattering curve fit has an *R* factor of 6.3% out to *Q* of 2.0 nm^{-1}, based on a curve measured at 14.3 mg/mL IgE-Fc. The neutron curve fit is compared with the X-ray scattering curve fit (dashed line). The IgE-Fc model is depicted in terms of stereo diagrams of both its α-carbon coordinates and the sphere model calculated from this, both drawn to the same scale.

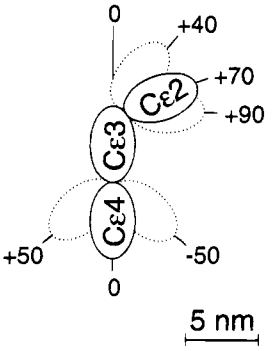

FIGURE 9: Schematic diagram of possible S-shaped and U-shaped models for IgE-Fc. The Cε2 domain is joined at an angle of 70° to the Cε3 domain by a short link. The ranges of rotation in the Cε2 and Cε4 domains (40° to 90°, and −50° to 50°, respectively) corresponding to the models within the lowest contour level in the $R_{2.0}$ contour plot of Figure 7 are denoted by dashed outlines.

this model is 3.22 nm as expected (see above), which is slightly less than the experimental value of 3.52 ± 0.12 nm. The R_{XS} value is 1.93 nm, which is within error of the observed value of 1.89 ± 0.05 nm. A cutoff value for $R_{2.0}$ of 4% (see Figure 7) suggests that the precision of this final model ranges between 40° and 90° for the Cε2−Cε3 bend angle, and ±50° for the Cε3−Cε4 bend angle (Figure 9). Figure 7 also shows that this minimum in $R_{2.0}$ correlates well with the other three parameters defining the outcome of the modeling.

This model was also compared with the experimental neutron scattering curve measured in ^2H_2O buffer. Despite the changes caused by the use of the currently-used empirical corrections for neutron beam divergence and wavelength spread (Mayans et al., 1995) and the use of an unhydrated model, this single-density model also resulted in a good curve fit in the *Q* range out to 1.5 nm^{-1} (Figure 8). Fits of similar quality were obtained for the concentration series between 3.6 and 14.3 mg/mL IgE-Fc. The neutron curve fit was distinct from that of the X-ray fit in reflection of the different physical conditions of the measurements, and the good agreement indicates the consistency of the modeling approach for IgE-Fc.

(e) Automated Hydrodynamic Simulations for IgE-Fc Models. Sedimentation coefficients provide a measure of macromolecular elongation that is complementary to the determination of R_G values for IgE-Fc. The four sets of 9360 sphere models were accordingly processed by means of hydrodynamic simulations in order to assess their compatibility with the published sedimentation coefficient of 4.7 ± 0.1 S for IgE-Fc (Keown et al., 1995). The calculated sedimentation coefficients in Table 3 show that, in all the sterically allowed domain models, $s^0_{20,w}$ varies in a range between 3.5 and 5.7 S. In the four sets of 100 best X-ray models in Table 3, this range is reduced to 3.8−5.1 S, and the average $s^0_{20,w}$ value is predicted to be 4.77 ± 0.12 S. This is in good agreement with experiment, and well within the expected precision of ±0.3 S for these simulations (Perkins, 1989; Perkins et al., 1993). This agreement is further support for the outcome of the AUTOSCT modeling procedure for the IgE-Fc domain structure. As $s^0_{20,w}$ and R_G values provide different physical measures of macro-

molecular elongation (Perkins, 1989), this agreement shows that the 0.3 nm difference between the experimental and modeled R_G values is not significant. The $s^0_{20,w}$ value of the model in Figure 8 is 4.77 S.

CONCLUSIONS

IgE binds to its high affinity receptor FcεRI on mast cells and basophils to trigger histamine release and to initiate an inflammatory response when cross-linked by allergens. The binding occurs between the Cε3 domain pair of IgE and the two immunoglobulin fold-like extracellular domains of the α-subunit of FcεRI (Sutton & Gould, 1993). The structure of IgE both free in solution and when bound to its receptor on the membrane has been investigated by measuring energy transfer between chromophores attached to the extremities of the IgE molecule (Zheng et al., 1991). These studies showed that IgE does not adopt an extended planar structure when either free or receptor-bound, but must be bent. This result is supported by solution scattering data on IgE (Davis et al., 1990; A. J. Beavil and S. J. Perkins, unpublished data). This structural asymmetry may account for the 1:1 stoichiometry of interaction between IgE and FcεRIα (Robertson, 1993; Sutton & Gould, 1993). Such a stoichiometry is important if IgE is not to cross-link receptor in the absence of allergen. More recently, it has been shown by analytical ultracentrifugation that IgE-Fc and the soluble extracellular fragment of FcεRIα (sFcεRIα) form a compact 1:1 complex (Keown et al., 1995). While this stoichiometry might be the result of steric hindrance with one sFcεRIα molecule preventing the binding of a second, it may again be due to a structural asymmetry in IgE-Fc. This study was accordingly performed in order to investigate the structure of the free IgE-Fc fragment, in particular with reference to the effect of the $(C\epsilon2)_2$ domain pair on the overall structure of IgE-Fc.

Two models of IgE-Fc have previously been proposed. In the first (1IGE; Padlan & Davies, 1986), the six domains adopt a compact planar arrangement with a "crossed" pairing of inter-heavy chain disulfide bridges which is now known to be incorrect. A second model with the correct "parallel" pairing was subsequently proposed (Figure 1; 2IGE; Helm et al., 1991), which results in a more extended linker region between the Cε2 and Cε3 domain in each chain. While this could lead to a very extended structure, Helm et al. (1991) pointed out that this linker region might allow the $(C\epsilon2)_2$ and $(C\epsilon3)_2$ domain pairs to adopt alternative orientations with respect to each other. This model was thus taken as the starting point for generating models to fit the experimental scattering data in the present study.

The study of the IgE-Fc fragment by solution scattering clearly shows that its overall structure is bent in solution. Curve fitting in the full Q range between Q of 0.13 and 2.0 nm^{-1} was necessary in order to achieve discrimination between bent and planar structures, for this was not possible on the basis of the experimental R_G and L data from Guinier analyses alone. The modeling analyses were based on the combination of calibrated procedures for scattering curve simulations from crystal structures (Smith et al., 1990; Perkins et al., 1993), the known crystal structure for the Fc fragment of IgG (Deisenhofer, 1981), and a good starting model for IgE-Fc (Helm et al., 1991). Neither the 1IGE nor the 2IGE planar models fitted the data, and attempts to bend the latter structure at the Cε2−Cε3 junction alone did not yield satisfactory agreement either. Even when bending at the Cε3−Cε4 junction was also considered (Figure 5f, good agreement was only achieved with extreme bending of 60−90° at this point. However, when the search was broadened by systematically investigating rotations and translations of all the domains (Figure 5b; Table 3), slight changes in the relative orientation of the two Cε3 domains by ±10° were found to have a significant effect on the curve fits (Figure 5e). The automated testing of 37 440 models showed that the requirement for extreme or indeed any bending at the Cε3−Cε4 junction was removed when the Cε3 domains were altered in this way. In summary, satisfactory models are bent at either the Cε2−Cε3 junction or the Cε3−Cε4 junction, or both. Models which do not incorporate a bend at the Cε2−Cε3 junction must be bent by 60−90° at the Cε3−Cε4 junction. Those which are not bent at the Cε3−Cε4 junction must be bent by at least 40−50° at the Cε2−Cε3 junction.

The bent model derived from X-ray scattering (Figure 8) is also consistent with preliminary hydrodynamic modeling of IgE-Fc (Keown et al., 1995) where a bend of 60−120° between the Cε2−Cε3 domains is required in the 2IGE model to account for its sedimentation coefficient. However, hydrodynamic modeling is limited by the same restrictions that apply to the use of R_G data to determine IgE-Fc models. Keown et al. (1995) were not able to exclude linear compact models for IgE-Fc from sedimentation coefficient data. It is important to note that solution scattering cannot define a single solution structure, nor even a single family of related structures (Glatter & Kratky, 1982). The use of known atomic structures for domains have however usefully constrained the types of structures under consideration. Figure 9 summarizes the outcome of this study, namely, a bent IgE-Fc structure, most probably at the Cε2−Cε3 junction, together with an indication of the permissible range of acceptable structures. Figure 9 includes both S-shaped and U-shaped models. However, if IgE-Fc has a bend at the Cε3−Cε4 junction, a U-shaped structure is more readily consistent with the fluorescence data of Zheng et al. (1991) and their bent model for the whole IgE molecule.

The final X-ray scattering models for IgE-Fc are stereochemically compatible with known distance constraints and crystal structures for the Fc fragment of IgG. In all 37 440 IgE-Fc models, the distance between the C-terminus of each domain and the N-terminus of the adjacent domain is such that the polypeptide connections can be made, as all the models are more compact than the starting model 2IGE. Helm et al. (1991) have noted that the extended linker region between the Cε2 and Cε3 domains (Figure 5b) could readily mediate bending of the IgE-Fc structure at this point. In contrast to this, the crystal structure determinations of free IgG-Fc (Deisenhofer, 1981; Sutton & Phillips, 1983) and IgG-Fc complexed with protein A, protein G, and neonatal Fc receptor (Deisenhofer, 1981; Sauer-Eriksson et al., 1995; Burmeister et al., 1994) indicate that there is no evidence for any substantial flexibility at the Cγ2−Cγ3 junction, which is homologous to the Cε3−Cε4 junction in IgE-Fc. This is not unexpected in view of the numerous interdomain interactions between the Cγ2 and Cγ3 domains in IgG-Fc and in the homologous models of IgE-Fc (Deisenhofer, 1981; Padlan & Davies, 1986; Helm et al., 1991). For these reasons we favor IgE-Fc models in Figures 6 and 7 in which IgE-Fc

is bent at the Cε2−Cε3 junction rather than at the Cε3−Cε4 junction. Such models have also been subjected to 10° rotations at the Cε3 domains. Although there is no precedent for such conformational differences with the IgG-Fc crystal structures, the Cγ2 domain pairs are all tethered in the same way in these structures by the inter-heavy chain disulfide bridge in the lower hinge region, whereas in IgE-Fc the $(C\epsilon2)_2$ domain pair and the linker segment between Cε2 and Cε3 provide an altogether different type of association. In fact, the crystal structure of hinge deleted IgG-Mcg does show that the Cγ2 domains adopt a different conformation and are pulled nearer together by the abnormally shorter connections to the Fab fragments (Guddat et al., 1993).

Why should IgE-Fc be bent? The binding site for FcεRI lies in the Cε3 domain, and the presence of the Cε2 domain is not required for this activity (Basu et al., 1993; H. J. Gould and B. J. Sutton, unpublished data). The asymmetric structure is therefore not required to generate the receptor binding site. Monovalency of IgE for FcεRI is certainly a functional necessity if receptor triggering in the absence of allergen is to be avoided, and the bent structure may ensure that each IgE molecule has only one accessible binding site. Indeed, the bent structure may have the effect of enhancing the affinity of the interaction by reducing steric occlusion of the site by the $(C\epsilon2)_2$ domain pair and Fab regions of IgE. This notion is supported by the approximate correlation between the relative affinities of the four subclasses of human IgG for their receptors FcγRI, FcγRII, or FcγRIII (IgG3 ≈ IgG1 > IgG4 ≈ IgG2; Ravetch & Kinet, 1991) and the lengths of their hinge regions; i.e., increased hinge length and reduced steric occlusion from the Fab fragments correlate with increased receptor affinity. The bent structure may therefore contribute to the uniquely high affinity of IgE for FcεRI.

This study indicates an interesting analogy between IgE and IgM with respect to the bending of these multidomain proteins. Both IgE and the IgM-S subunit of IgM have the same number of domains and the same length of linker between these domains. IgM-S has a C-terminal tailpiece and additional Cys residues that mediate the formation of pentameric or hexameric IgM. In solution, IgM is essentially planar, as predicted from its appearance in electron micrographs and as observed directly by X-ray scattering (Perkins et al., 1991). However, when bound to an antigenic surface, the IgM structure is dislocated with the Fab fragments bent relative to the central Fc region (Feinstein et al., 1986). X-ray scattering of the Fab_2 fragment of IgM (which consists of the two Fab fragments linked by the $(C\mu2)_2$ domain pair) indicated that this formed a relatively rigid unit (Perkins et al., 1991). Dislocation is thus more likely to occur at the Cμ2-Cμ3 junction, which is homologous to the Cε2−Cε3 junction in IgE. It is only in the dislocated form that IgM can bind to C1q and activate complement, for which the binding site involves Cμ3 residues that are proximal to the Cμ2−Cμ3 junction (Perkins et al., 1991; Arya et al., 1994). The bend in IgE-Fc may similarly serve to expose the high affinity receptor binding site, part of which lies in a homologous location in the Cε3 domain.

The present development of an automated method of domain searches constrained by known atomic structures for arrangements that fit the X-ray scattering curves of multidomain proteins has been of great value for IgE-Fc. The automated modeling of IgE-Fc was intended to determine the following: (i) which domain movements are distinguishable by solution scattering; (ii) if a single conformation or family of models could be obtained; and (iii) how unique any structure is. The results of Table 3 and Figure 7 show that all these objectives were realized. A simplified version of this approach was useful for the automated fitting of neutron scattering curves for IgG (Mayans et al., 1995). While it is necessary to expend effort in setting up a modeling search protocol, the tedium of performing manual searches for models that fit scattering curves is no longer required. The time saved in generating curve fits is substantial, different types of postulated models can be readily evaluated, the quality of the curve modeling is much improved, and the models can be directly tested against hydrodynamic frictional coefficients. It is possible to define error ranges on the precision of models generated by this procedure. Ultimately, what will be of interest is the comparison of the best-fitting IgE-Fc models with a crystal structure for IgE-Fc if this becomes available, as this will indicate the extent to which this automated procedure has worked.

ACKNOWLEDGMENT

We thank Professor H. J. Gould for useful discussions. We thank Dr. R. J. Owens (Celltech Ltd.) for assistance with the IgE-Fc preparations, Dr. R. L. Beavil for computer artwork, the Engineering and Physical Sciences Research Council for access to X-ray and neutron facilities, and Dr. W. Bras (SRS), Dr. R. K. Heenan (ISIS) and Dr. S. M. King (ISIS) for generous instrumental support.

REFERENCES

Arya, S., Chen, F., Spycher, S., Isenman, D. E., Shulman, M. J., & Painter, R. H. (1994) *J. Immunol., 152*, 1206−1212.

Ashton, A. W., Kemball-Cook, G., Johnson, D. J. D., Martin, D. M. A., O'Brien, D. P., Tuddenham, E. D. G., & Perkins, S. J. (1995) *FEBS Lett.* (in press).

Basu, M., Hakimi, J., Dharm, E., Kondas, J. A., Tsien, W.-H., Pilson, R. S., Lin, P., Gilfillon, A., Haring, P., Braswell, E. H., Nettleton, M. Y., & Kochan, J. P. (1993) *J. Biol. Chem. 268*, 13118−13127.

Beavil, A. J., Beavil, R. J., Chan, C. M. W., Cook, J. P. D., Gould, H. J., Henry, A. J., Owens, R. J., Shi, J., Sutton, B. J., & Young, R. J. (1993) *Biochem. Soc. Trans. 21*, 968−972.

Burmeister, W. P., Huber, A. H., & Bjorkman, P. J. (1994) *Nature (London) 372*, 379−383.

Chothia, C. (1975) *Nature (London) 254*, 304−308.

Davis, K. G., Glennie, M., Harding, S. E., & Burton, D. R. (1990) *Biochem. Soc. Trans. 18*, 935−936.

Deisenhofer, J. (1981) *Biochemistry 20*, 2361−2370.

Feinstein, A., Richardson, N., & Taussig, M. J. (1986) *Immunol. Today 7*, 169−174.

Garcia de la Torre, J. (1989) In *Dynamic Properties of Biomolecular Assemblies* (Harding, S. E., & Rowe, A. J., Eds.) pp 3−31, Royal Society of Chemistry, Cambridge.

Garcia de la Torre, J., & Bloomfield, V. A. (1977a) *Biopolymers 16*, 1747−1761.

Garcia de la Torre, J., & Bloomfield, V. A. (1977b) *Biopolymers 16*, 1779−1793.

Glatter, O., & Kratky, O., Eds. (1982) *Small-angle X-ray scattering*, Academic Press, New York.

Guddat, L. W., Herron, J. N., & Edmundson, A. B. (1993) *Proc. Natl. Acad. Sci. U.S.A. 90*, 4271−4275.

Heenan, R. K., & King, S. M. (1993) *Proceedings of an International Seminar on Structural Investigations at Pulsed Neutron Sources*, Dubna, Sept 1−4, 1992. Report E3-93-65. Joint Institute for Nuclear Research, Dubna.

Heenan, R. K., King, S. M., Osborn, R., & Stanley, H. B. (1989) *Colette Users Guide*. Internal Publication RAL-89-128, Rutherford Appleton Laboratory, Didcot, U.K.
Helm, B. A., Marsh, P., Vercelli, D., Padlan, E. A., Gould, H. J., & Geha, R. (1988) *Nature 331*, 180−183.
Helm, B. A., Ling, Y., Teale, C., Padlan, E. A., & Brüggemann, M. (1991) *Eur. J. Immunol. 21*, 1543−1548.
Hjelm, R. J. (1985) *J. Appl. Crystallogr. 18*, 452−460.
Holowka, D., Wensel, T., & Baird, B. (1990) *Biochemistry 29*, 4607−4612.
Keown, M. B., Ghirlando, R., Young, R. J., Beavil, A. J., Owen, R. J., Perkins, S. J., Sutton, B. J., & Gould, H. J. (1995) *Proc. Natl. Acad. Sci. U.S.A. 92*, 1841−1845.
Kratky, O. (1963) *Prog. Biophys. Chem. 13*, 105−173.
Mayans, M. O., Coadwell, W. J., Beale, D., Symons, D. B. A., & Perkins, S. J. (1995) *Biochem. J. 311*, 283−291.
Nissim, A., Jouvain, M.-H., & Eshhar, Z. (1991) EMBO *J. 10*, 101−107.
Nissim, A., Schwarzbaum, S., Siraganian, R., & Eshar, Z. (1993) *J. Immunol. 150*, 1365−1374.
Padlan, E. A., & Davies, D. R. (1986) *Mol. Immunol. 23*, 1063−1075.
Perkins, S. J. (1986) *Eur. J. Biochem. 157*, 169−180.
Perkins, S. J. (1988) In *New Comprehensive Biochemistry* (Neuberger, A., & Van Deenen, L. L. M., Eds.) Vol. 11B, Part II, pp 143−264, Elsevier, Amsterdam.
Perkins, S. J. (1989) In *Dynamic Properties of Biomolecular Assemblies* (Harding, S. E., & Rowe, A. J., Eds.) Chapter 15, pp 226−245, Royal Society of Chemistry, London.
Perkins, S. J. (1994) In *Physical Methods of Analysis* (Jones, C., Mulloy, B., & Thomas, A. H., Eds.) Methods in Molecular Biology, Vol. 22, pp 39−60, Humana, Totowa, NJ.
Perkins, S. J., & Weiss, H. (1983) *J. Mol. Biol. 168*, 847−866.
Perkins, S. J., Nealis, A. S., Sutton, B. J., & Feinstein, A. (1991) *J. Mol. Biol. 221*, 1345−1366.
Perkins, S. J., Smith, K. F., Kilpatrick, J. M., Volanakis, J. E., & Sim, R. B. (1993) *Biochem. J. 295*, 87−99.
Pilz, I. (1973) In *Physical Principles and Techniques of Protein Chemistry* (Leach, S. J., Ed.) Part C, Chapter 19, 141−243, Academic Press, New York.
Pilz, I., Kratky, O., Licht, A., & Sela, M. (1973) *Biochemistry 12*, 4998−5005.
Presta, L., Shields, R., O'Connell, L., Lahr, S., Porter, J., Gorman, C., & Jardieu, P. (1994) *J. Biol. Chem. 269*, 26368−26373.
Rademacher, T. W., Homans, S. W., Fernandes, D. L., Dwek, R. A., Mizuochi, T., Taniguchi, T., & Kobata, A. (1983) *Biochem. Soc. Trans. 11*, 132−134.
Ravetch, J. V., & Kinet, J.-P. (1991) *Annu. Rev. Immunol. 9*, 457−492.
Robertson, M. W. (1993) *J. Biol. Chem. 268*, 12736−12743.
Sauer-Eriksson, A. E., Kleywegt, G. J., Uhlen, M., & Jones, T. A. (1995) *Structure 5*, 265−278.
Semenyuk, A. V., & Svergun, D. I. (1991) *J. Appl. Crystallogr. 24*, 537−540.
Sherr, E., Macy, E., Kimata, H., Gilly, M., & Saxon, A. (1989) *J. Immunol. 142*, 481−489.
Smith, K. F., Harrison, R. A., & Perkins, S. J. (1990) *Biochem. J. 267*, 203−212.
Sutton, B. J., & Phillips, D. C. (1983) *Biochem. Soc. Trans. 11*, 130−132.
Sutton, B. J., & Gould, H. J. (1993) *Nature 366*, 421−428.
Svergun, D. I. (1992) *J. Appl. Crystallogr. 25*, 495−503.
Svergun, D. I., Semenyuk, A. V., & Feigin, L. A. (1988) *Acta Crystallogr. A44*, 244−250.
Towns-Andrews, E., Berry, A., Bordas, J., Mant, G. R., Murray, P. K., Roberts, K., Sumner, I., Worgan, J. S., Lewis, R., & Gabriel, A. (1989) *Rev. Sci. Instrum. 60*, 2346−2349.
Weetall, M., Shopes, B., Holowoka, D., & Baird, B. (1990) *J. Immunol. 145*, 3849−3854.
Wignall, G. D., & Bates, F. S. (1987) *J. Appl. Crystallogr. 20*, 28−40.
Williams, A. F., & Barclay, A. N. (1988) *Annu. Rev. Immunol. 6*, 381−405.
Worgan, J. S., Lewis, R., Fore, N. S., Sumner, I. L., Berry, A., Parker, B., D'Annunzio, F., Martin-Fernandez, M. L., Towns-Andrews, E., Harries, J. E., Mant, G. R., Diakun, G. P., & Bordas, J. (1990) *Nucl. Instrum. Methods Phys. Res. A291*, 447−454.
Young, R. J., Owens, R. J., Mackay, G. A., Chan, C. M. W., Shi, J., Hide, M., Francis, D. M., Henry, A. J., Sutton, B. J., & Gould, H. J. (1995) *Protein Eng. 8*, 193−199.
Zheng, Y., Shopes, B., Holowka, D., & Baird, B. (1991) *Biochemistry 30*, 9125−9132.
Zheng, Y., Shopes, B., Holowka, D., & Baird, B. (1992) *Biochemistry 31*, 7446−7456.

BI951410G